Supporting Information

Conversion of layered materials to ultrathin amorphous nanosheets induced by ball-milling insertion and pure-water exfoliation

Chao Deng, Yuxuan Gao, Yingbang Yao, Bo Liang, Shengguo Lu, Tao Tao*

Corresponding author：

taotao@gdut.edu.cn

Materials and Methods

1   Alkali metal-based layered materials.

54.0 g of iron balls with various diameters and 0.5 g of commercial layered materials (BN, V_2O_5, graphite, WS_2, MoS_2, or their composites) were placed into a ball mill container, heated at 100 °C for 1 hour in a vacuum oven, quickly moved into the transportation chamber of an argon-filled glove box (oxygen and moisture level below than 0.1 ppm), and naturally cooled under vacuum for 2 hours to remove the residual air from the container. Then six slices of alkali metal foils (Li, Na, or K) were cut into small pieces (about 0.265 grams), loaded inside the container with layered materials and iron ball, and sealed in the argon-filled glove box. The diameters of iron ball and ball milling time are different for the treatment of different layered materials: 10 mm (3.6 g×15) and 48 h for BN (1 μm, Macklin, 98.5 %) and $BN/V_2O_5/C$, 10 mm (3.6 g×5), 8 mm (2.0 g×18) and 96 h for graphite (Aladdin, 98.0%) and $BN/MoS_2/C$, 10 mm (3.6 g×5), 8 mm (2.0 g×9), 5 mm (0.5 g×36) and 48 h for V_2O_5 (Aladdin, 99.0%), and 10 mm (3.6 g×5), 5 mm (0.5 g×40), 3 mm (0.1 g×160) and 48h for MoS_2 (12-16 μm, Macklin, 99.9%), WS_2 (2 μm, Macklin, 99.9 %) , BN/C, MoS_2/C, WS_2/C, and V_2O_5/C. All the mixtures of Li foils, Na foils or K foils and layered materials were milled at a rotation speed of 700 rpm by FRITSCH P7 at room temperature under argon atmosphere.

2   Preparation of ultrathin amorphous nanosheets.

Ultrathin amorphous nanosheets were obtained from the milled composite powder by the following hydrothermal treatment in pure water (60 °C). 1 mg of the milled composite powder and a stirring rod were loaded into a 150 mL beaker in the argon-filled glove box. When the beaker was moved out from the glove box, distilled water (60 °C, 100 mL) was immediately added into the beaker to treat the milled composite powder. Then the solution with the powder was further stirred for 30 min. After reaction, the solution was filtered and washed by 100 ml water, and the obtained solid samples dried at 60 °C for 12 h.

3 Preparation of amorphous nanosheets modified Celgard separators.

To improve the wettability of Celgard separators, the above-mentioned solution with the powder was taken and mixed with absolute ethanol. The mixture of the upper solution (50 mL) and absolute ethanol (50 mL) was stirred for 1-2 min, fully transferred to a flask of suction filtration covered with the bare Celgard separators, and dried for 12 h at 80 °C to prepare the amorphous nanosheets modified Celgard separators. To slow down the leakage speed of solution and ensure a uniform distribution of nanosheets on the surface of separator, the flask bottom of suction filtration was firstly covered with a layer of aluminum foil paper, and coupled with a layer of separator before solution transferring.

4 Materials characterization.

The morphology and element distribution of samples were examined by a scanning electron microscopy (SEM, Hitachi Co., SU8220), field-emission scanning electron microscope (FESEM, Hitachi Co., SU8220) and X-ray Photoelectron Spectroscopy (XPS) (Thermo Fisher Co., Escalab 250Xi). X-ray diffraction (XRD) analysis was performed over the range of 10-90° with a scanning rate of 10° per min on a Bruker D8 Advance , transmission electron microscope (TEM) analysis on an FEI Co., Talos F200S and a Hitachi HT7700, Raman analysis by Qontor (Renishaw, UK) with 532 nm laser, and the Fourier Transform Infrared spectroscopy (FTIR) by NICOLET 6700 FT-IR Spectrometer (Thermo) from wave-number 500 to 4000 cm^{-1}. The thickness of 2D nanosheets was measured by an Atomic force microscope (AFM) (Dimension FastScan, Bruker Co.), and the mechanical properties using the electronic universal testing machine (TableBlue 5KN, Hegewald&Peschke, Germany) at a stretching speed of 60 mm min^{-1} with samples approximately 5.5 cm wide and 9.0 cm long. A flash thermal conductivity meter (LFA 447, Netzsch, Germany) was used to measure the thermal diffusivity of the sample, and the test temperature was 25 °C. Using a thermogravimetric-differential thermal analyzer (DSC-

TGA SDT 2960, TA, America) to measure the heat capacity of the sample, and the measurement temperature is 25 °C and the heating rate is 10 °C min^{-1}.

5 Electrochemical characterization.

CR2032 coin-type cells composed of liquid electrolyte, separators or the modified separators and S based cathodes were assembled with lithium metal foils in the argon glove box. The S based cathode material is the composite of 80 wt.% S-graphene(70 wt.% S; 30 wt.% Graphene), 10 wt.% PVDF and 10 wt.% Super P carbon black. The liquid electrolytes were 1.0 M LiTFSI in 1:1 v/v 1, 3-dioxolane/1, 2-dimethoxyethane with LiNO$_3$. The cells were galvanostatically discharged-charged by using a LAND battery tester (Wuhan LAND Co., China) at various current densities at room temperature under a voltage window of 1.6-2.8 V.
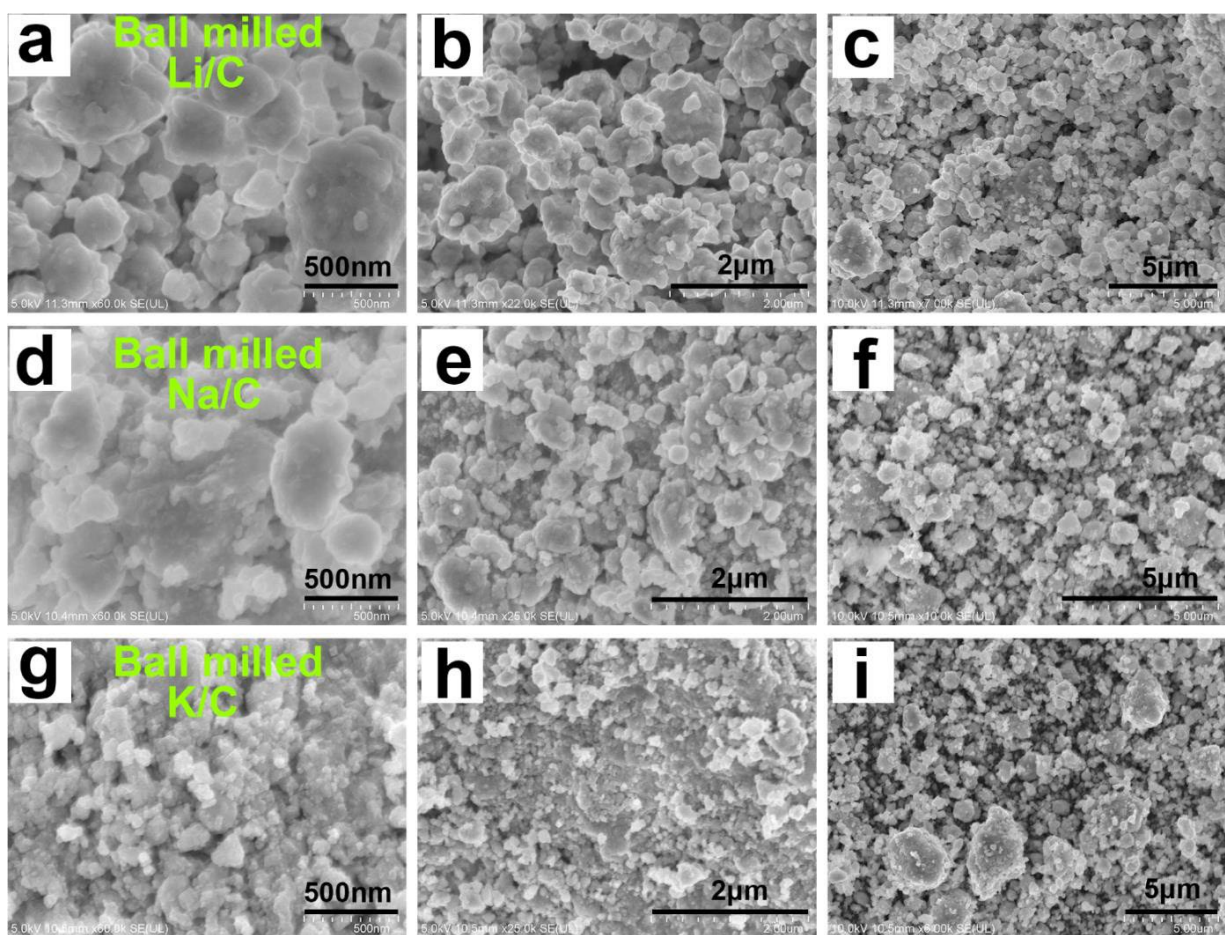

Fig. S1. SEM images of (a-c) the 96 h milled Li/C composite powder, (d-f) the 48 h milled Na/C composite powder, and (g-i) the 48 h milled K/C composite powder.
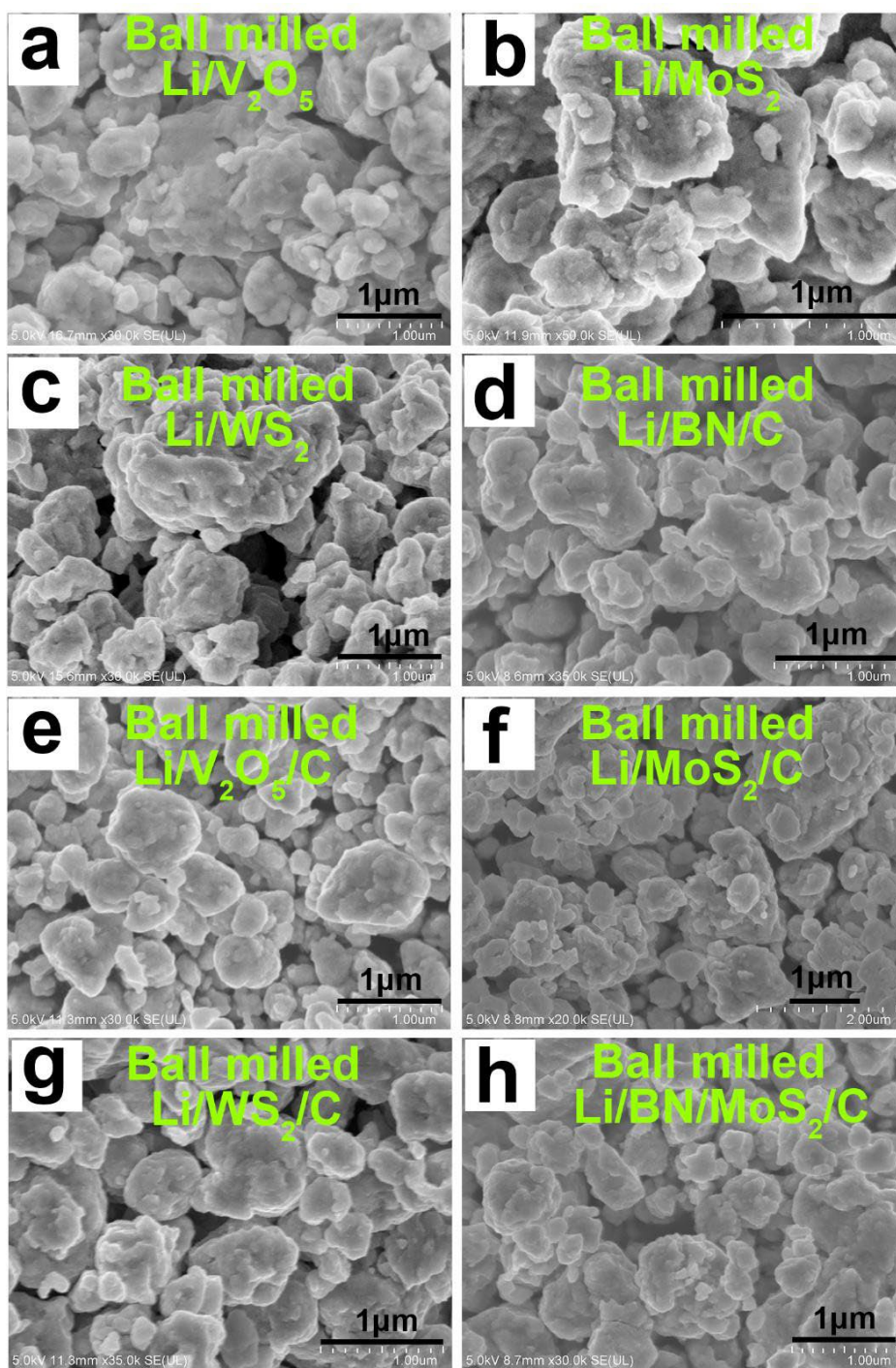
a Ball milled Li/V$_2$O$_5$
1μm

b Ball milled Li/MoS$_2$
1μm

c Ball milled Li/WS$_2$
1μm

d Ball milled Li/BN/C
1μm

e Ball milled Li/V$_2$O$_5$/C
1μm

f Ball milled Li/MoS$_2$/C
1μm

g Ball milled Li/WS$_2$/C
1μm

h Ball milled Li/BN/MoS$_2$/C
1μm

Fig. S2. SEM images of (a) the 48 h milled Li/V$_2$O$_5$ composite powder, (b) the 48 h milled Li/MoS$_2$ composite powder, (c) the 48 h milled Li/WS$_2$ composite powder, (d) the 48 h milled Li/BN/C composite powder, (e) the 48 h milled Li/V$_2$O$_5$/C composite powder, (f) the 48 h milled Li/MoS$_2$/C composite powder, (g) the 48 h milled Li/WS$_2$/C composite powder, and (h) the 96 h milled Li/BN/MoS$_2$/C composite powder.
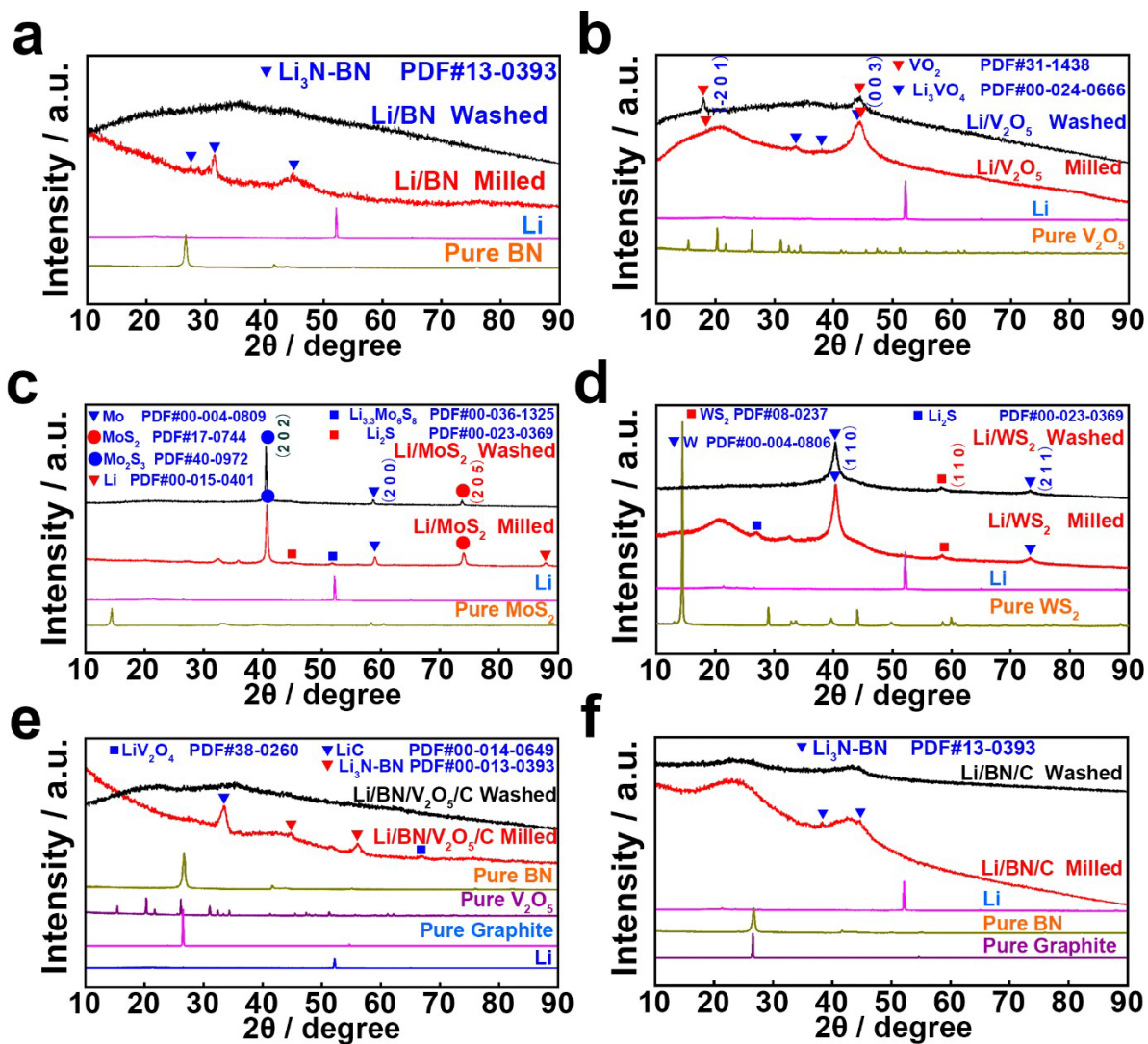
Fig. S3. XRD patterns of the milled composite powder and their washed product. (a) Li/BN, (b) Li/V_2O_5, (c) Li/MoS_2, (d) Li/WS_2, (e) Li/ BN/V_2O_5/C, and (f) Li/BN/C, respectively.
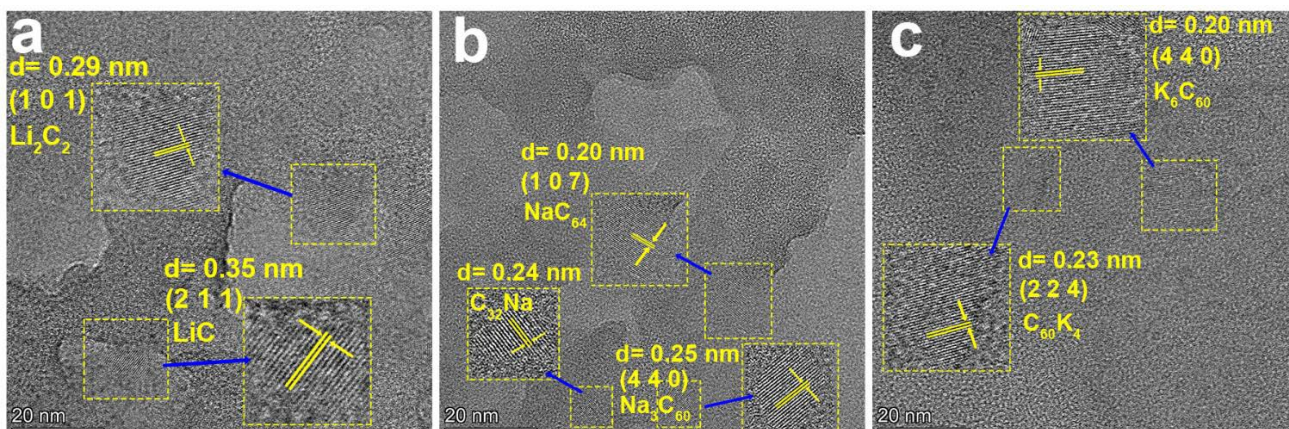
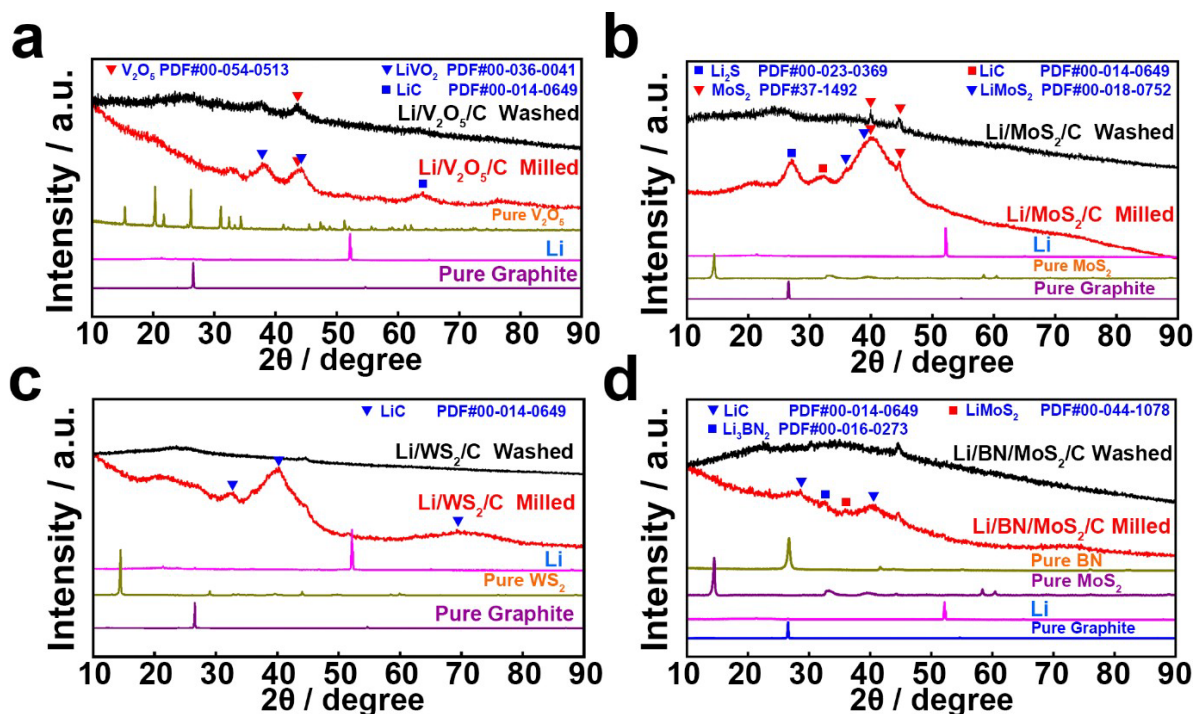**Fig. S4.** (a-c) HRTEM images of the milled composite powder. (a) Li/C, (b) Na/C, (c) K/C, respectively.

Fig. S5. XRD patterns of the milled composite powder and their washed product. (a) Li/V_2O_5/C, (b) Li/MoS_2/C, (c) Li/WS_2/C, and (d) Li/BN/MoS_2/C, respectively.
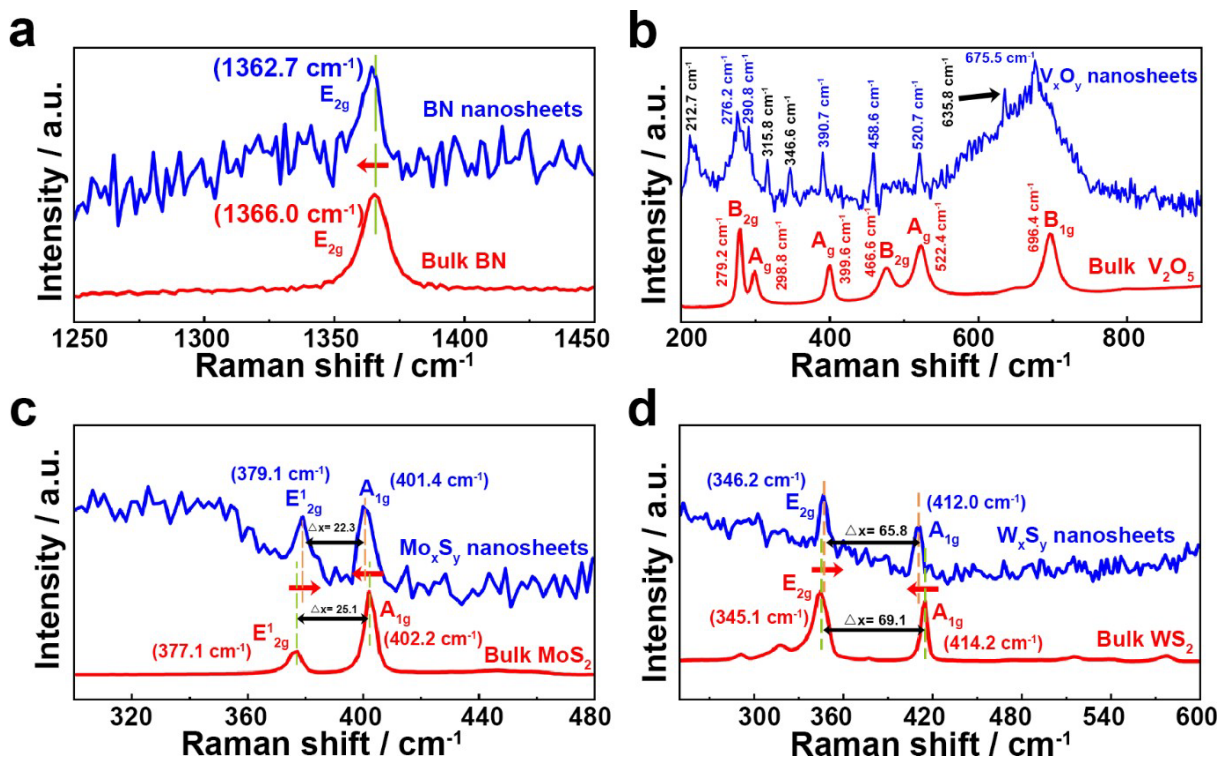
Fig. S6. Raman spectra of the nanosheets. (a) BN, (b) V_xO_y, (c) Mo_xS_y, and (d) W_xS_y nanosheets, respectively.

In Raman spectra of BN nanosheets (Fig. S6a), peaks shift down to low wavenumbers, the principal interlayer Raman active E_{2g} mode of BN is located at 1366 cm^{-1}, and single layer and few-layered BN nanosheets have a red-shift.[1]

The Raman Spectrum of the V_xO_y nanosheets as well as the bulk V_2O_5 were shown in Fig. S6b, the typical peaks of bulk V_2O_5 ($\sim$279.2, 298.8, 399.6, 466.6, 522.4 and 696.5 cm^{-1}) were observed.[2] For V_xO_y nanosheets (Fig. S6b), the Raman shift corresponds to different modes of vibrations are 276.2, 290.8, 390.7, 458.6, 520.7 and 674.3 cm^{-1}, and the Raman spectra are slightly shifted. The emergence of new peaks (212.7, 315.8, 346.6 and 635.8 cm^{-1}), can be due to the formation of VO_2.

The Raman spectrum of Mo_xS_y nanosheets (Fig. S6c) show two distinct characteristic peaks assignable to E^1_{2g} and A_{1g} bands at about 379.1 and 401.4 cm^{-1}, respectively, which are sensitive to changes in number of layers.[3] The broad absorption peaks of 379.1 and 401.4 cm^{-1} could be due to the overlapping of both MoS_2 and Mo_2S_3 species.[4] As the number of layers decreases, the weakened interlayer van der Waals forces in MoS_2 reduce the

8

binding of the atomic vibrations, leading to higher force constants, which result in a lower frequency of the A_{1g} peak. In contrast, the E^1_{2g} peak shows a blue shift, suggesting that increased interlayer van der Waals forces play a secondary role, while structural changes due to stacking or long-range Coulomb interlayer interactions in multilayer MoS_2 may dominate the changes in atomic vibrations. Therefore, the apparent peak shift and the significant change in peak difference indicate that the layer number of the prepared Mo_xS_y nanosheets is less than four.[5]

Fig. S6d shows that the softening of the A_{1g} (412.0 cm^{-1}) mode of W_xS_y nanosheets is less than that of bulk WS_2 (414.2 cm^{-1}), resulting from weaker interlayer contributions to the phonon restoring forces. The E_{2g} and A_{1g} patterns of the WS_2 nanosheets occur at 346.2 cm^{-1} and 412.0 cm^{-1}, respectively. In contrast, the two patterns of bulk WS_2 are located at 345.1 cm^{-1}(E_{2g}) and 414.2 cm^{-1} (A_{1g}). The shift in the A_{1g} and E_{2g} modes for the exfoliated layers compared to those of bulk clearly indicate softening of A_{1g} and E_{2g} modes and phonon confinement that is expected for single to few layer WS_2. This suggests that W_xS_y nanosheets were successfully prepared.
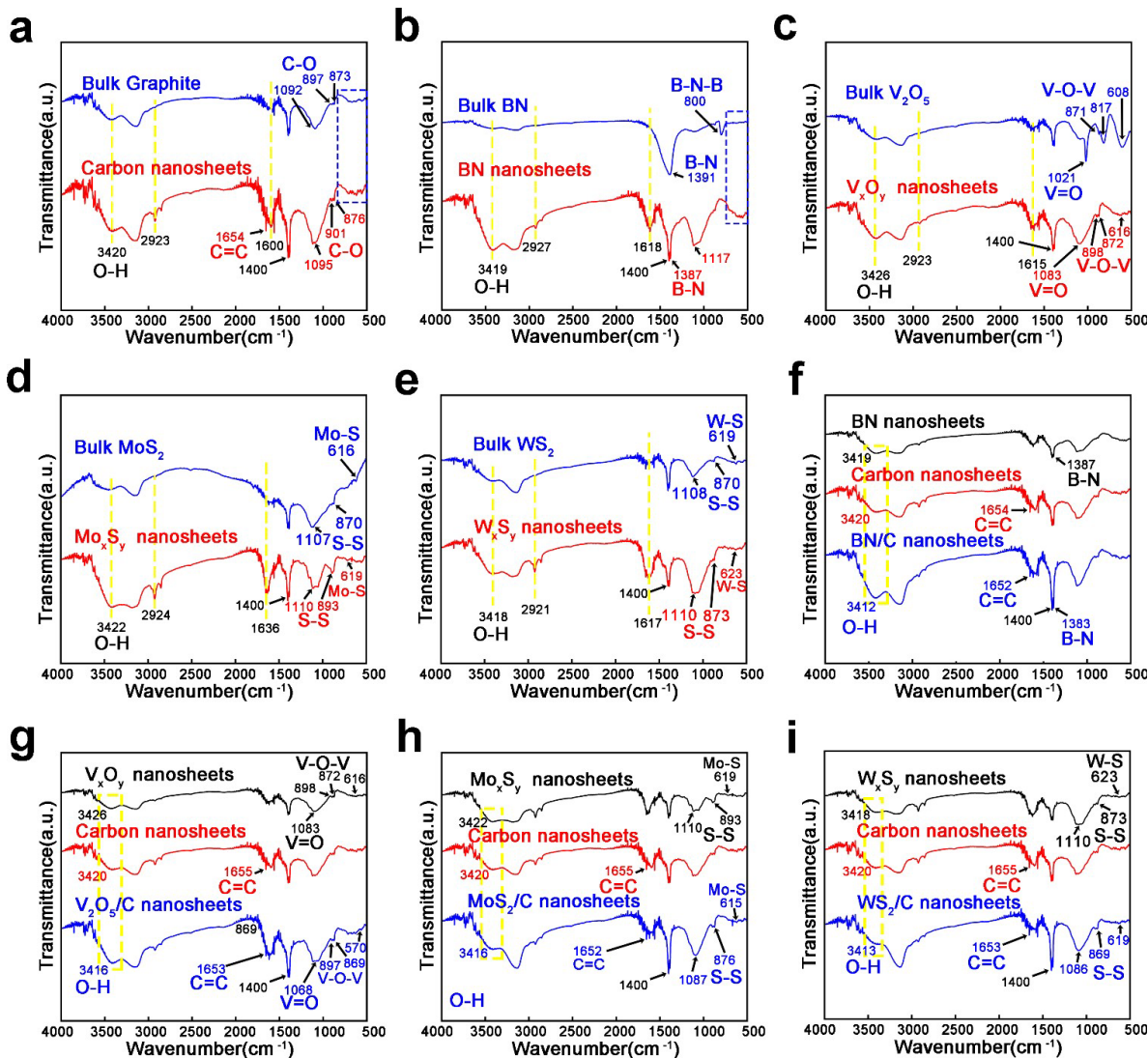
Fig. S7. FT-IR spectra of the nanosheets. (a) Carbon, (b) BN, (c) V_xO_y, (d) Mo_xS_y, (e) W_xS_y, (f) BN/C, (g) V_2O_5/C, (h) MoS_2/C, and (i) WS_2/C nanosheets, respectively.

Due to the transformation of layered materials structure from bulk to 2D nanosheets, the intensity and position of some peaks in FT-IR spectra have an obvious change, several peaks disappear, and several new peaks appear.

In comparison with that of bulk graphite, C=C bond of carbon nanosheets (Fig. S7a) can be observed in the range of 1654 cm^{-1}, and C=C at 1654 cm^{-1} can be assigned to skeletal vibrations of unoxidized graphitic domains.[6] The C-O bond (1092, 897, and 873 cm^{-1}) of carbon nanosheets shifts to the higher peak position, and several different infrared spectrum peaks can be observed in the range of 500-700 cm^{-1}. The relatively strong peaks of carbon nanosheets centered at about 3420, 2923 and 1600 cm^{-1} can are ascribed to the stretching of the O-H groups. In Fig. S7b, The two characteristic bands of B-N-B and B-

N at 800 and 1391 cm^{-1} are commonly shared with bulk BN, In contrast, the intensity of peaks at about 3419, 2927 and 1618 cm^{-1} are notably enhanced, an additional peak at 1117 cm^{-1} for BN nanosheets can be ascribed to the stretching of the O-H and B-O groups, respectively,[7] and several shifted infrared spectrum peaks are observed in the range of 500-715 cm^{-1}. Also, the peak position is slightly shifted from 1391 cm^{-1} to 1387 cm^{-1}.

In comparison with that of bulk V_2O_5, the intensity of peaks at about 3426, 2923 and 1615 cm^{-1} is notably enhanced for V_xO_y nanosheets (Fig. S7c), which is ascribed to the stretching of the O-H groups, respectively. In bulk V_2O_5, the bands at 871, 817 and 608 cm^{-1} are assigned to V-O, respectively, and the absorptions at wave numbers about 1021 cm^{-1} are associated to the V=O band.[8] But in V_xO_y nanosheets, V=O is shifted to 1083 cm^{-1} and V-O is shifted to 898, 872, 616 cm^{-1}. In bulk MoS_2, the sharp and narrow peak at 616 cm^{-1} can be assigned to the stretching vibration of the Mo-S bond, and peaks near 870 and 1107 cm^{-1} indicating S-S characteristics stretching respectively. In Mo_xS_y nanosheets (Fig. S7d), the wide absorption peaks at 3422, 2924 and 1636 cm^{-1} are clearly assignable as the stretching vibration of O-H. The Mo-S bond and S-S band shifts to the higher peak position.

In Fig. S7e, The peaks at 619 and 1108, 870 cm^{-1} correspond to W-S and S-S bonds,[9] respectively. The peaks at 1617 cm^{-1} represent hydroxyl groups and peaks at 2921 and 3418 cm^{-1} are related to the O-H bond.[10] The W-S bond and S-S band shifts to the higher peak position, and the peak of S-S band is broaden. Several different infrared spectrum peaks can be observed in the range of 500-810 cm^{-1}.

In the BN/C heterostructure nanosheets (Fig. S7f), the peak at 1652 cm^{-1} (C=C) is correlated with the carbon nanosheets, and 1383 cm^{-1} (B-N) confirms the existence of BN nanosheets. In contrast, the shifted position of absorption peaks (1652 cm^{-1}, 1383 cm^{-1}, and 3412 cm^{-1}), and the increase of peak intensity, could be attributed to the appearance of O-H groups and preparation of heterostructure nanosheets.[11]

V_2O_5/C heterostructure nanosheets spectra (Fig. S7g) exhibit extra characteristic peaks at 1653 cm^{-1} (C=C), and 3416 cm^{-1} (O-H groups), and its intensity signicantly increases. In Fig. S7h, as compared to the MoS_2 nanosheets and carbon nanosheets, the appearance of peaks at 1652 cm^{-1} (C=C), 3420 and 3422 cm^{-1} (O-H groups), increase of peak intensity, appearance of several new peaks in the range of 500 to 850 cm^{-1} (C-S bond),[12] and shift of

peak position (C=C, S-S and Mo-S band), could be attributed to the emergence of hetero-structure nanosheets. In the WS$_2$/C heterostructure nanosheets (Fig. S7i), the spectra exhibit extra characteristic peaks at 1654 cm^{-1} (C=C), 3413 cm^{-1}(O-H groups), and the difference peaks in the range of 500 to 833 cm^{-1} (C-S bond).
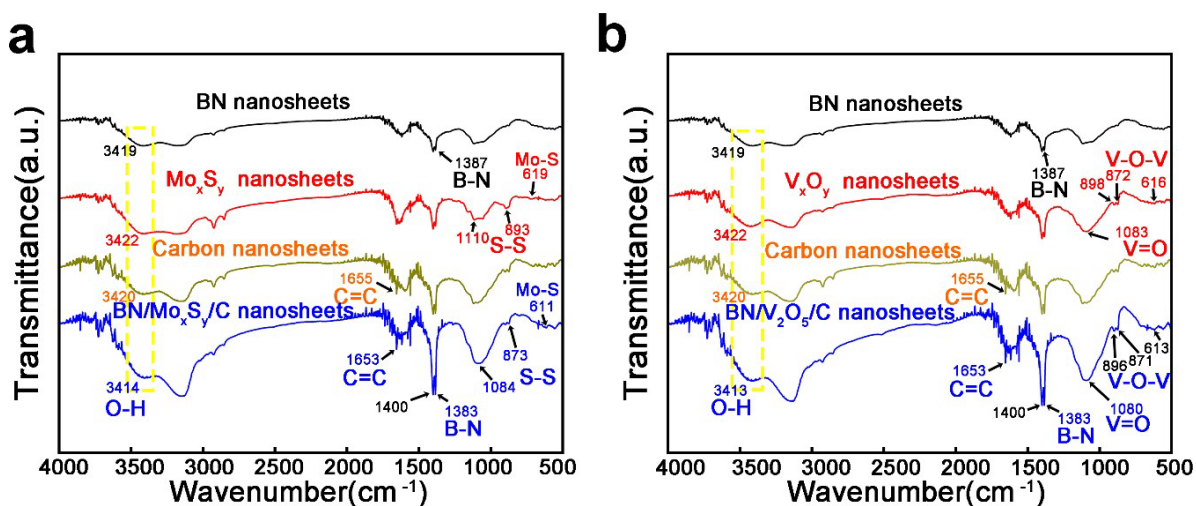

Fig. S8. FT-IR spectra of the nanosheets. (a) BN/Mo$_x$S$_y$/C, and (b) BN/V$_2$O$_5$/C nanosheets, respectively.

The FT-IR spectra of BN/Mo$_x$S$_y$/C heterostructure nanosheets (Fig. S8a) show characteristic peaks at 1653 cm^{-1} (C=C), 1383 cm^{-1}(B-N), 3414 cm^{-1} (O-H groups), and the difference peaks in the range of 500 to 850 cm^{-1} (C-S bond). In Fig. S8b, the FT-IR spectra of BN/V$_2$O$_5$/C heterostructure nanosheets show characteristic peaks at 1653 cm^{-1} (C=C), 1383 cm^{-1}(B-N), 3413 cm^{-1} (O-H groups), and the difference peaks in the range of 500 to 870 cm^{-1} (C-S bond). The peaks correlated with the O-H bands for at all nanosheets or heterostructure nanosheets can be ascribed to the water adsorbed on the surface of the as-prepared samples during water exfoliation process.
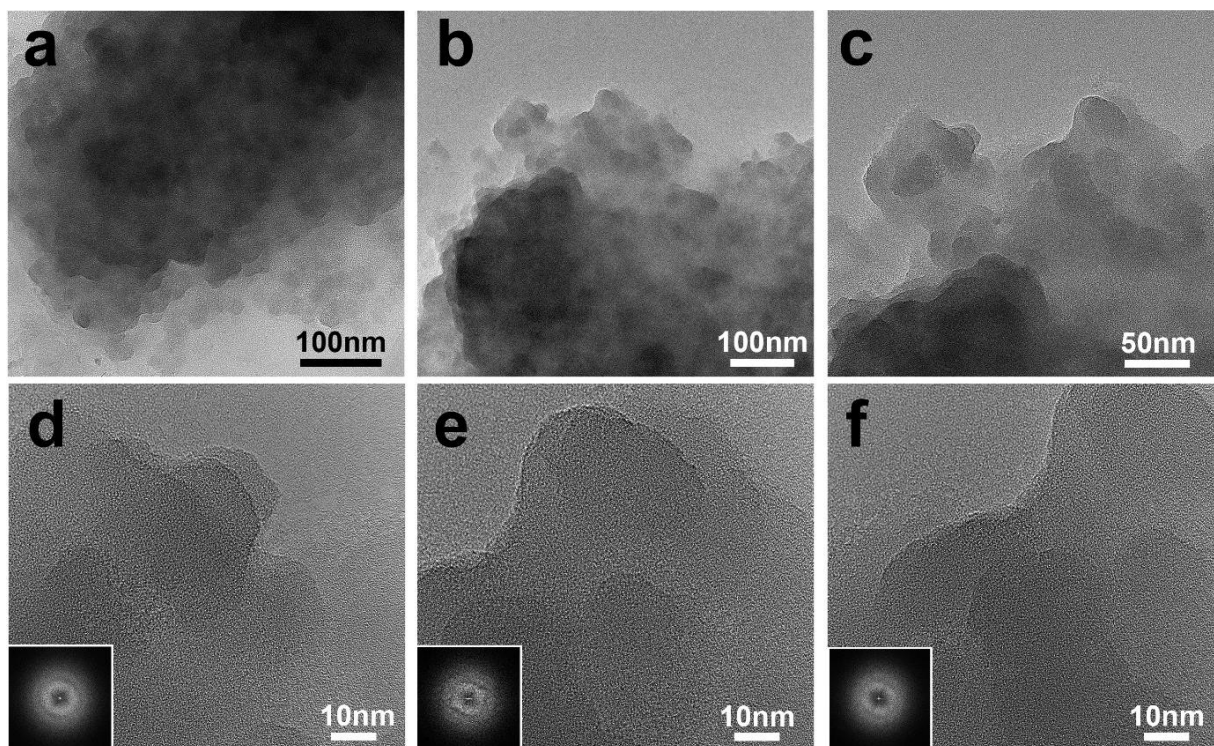
Fig. S9. (a-f) TEM and HRTEM images of the obtained $BN/V_2O_5/C$ nanosheets.
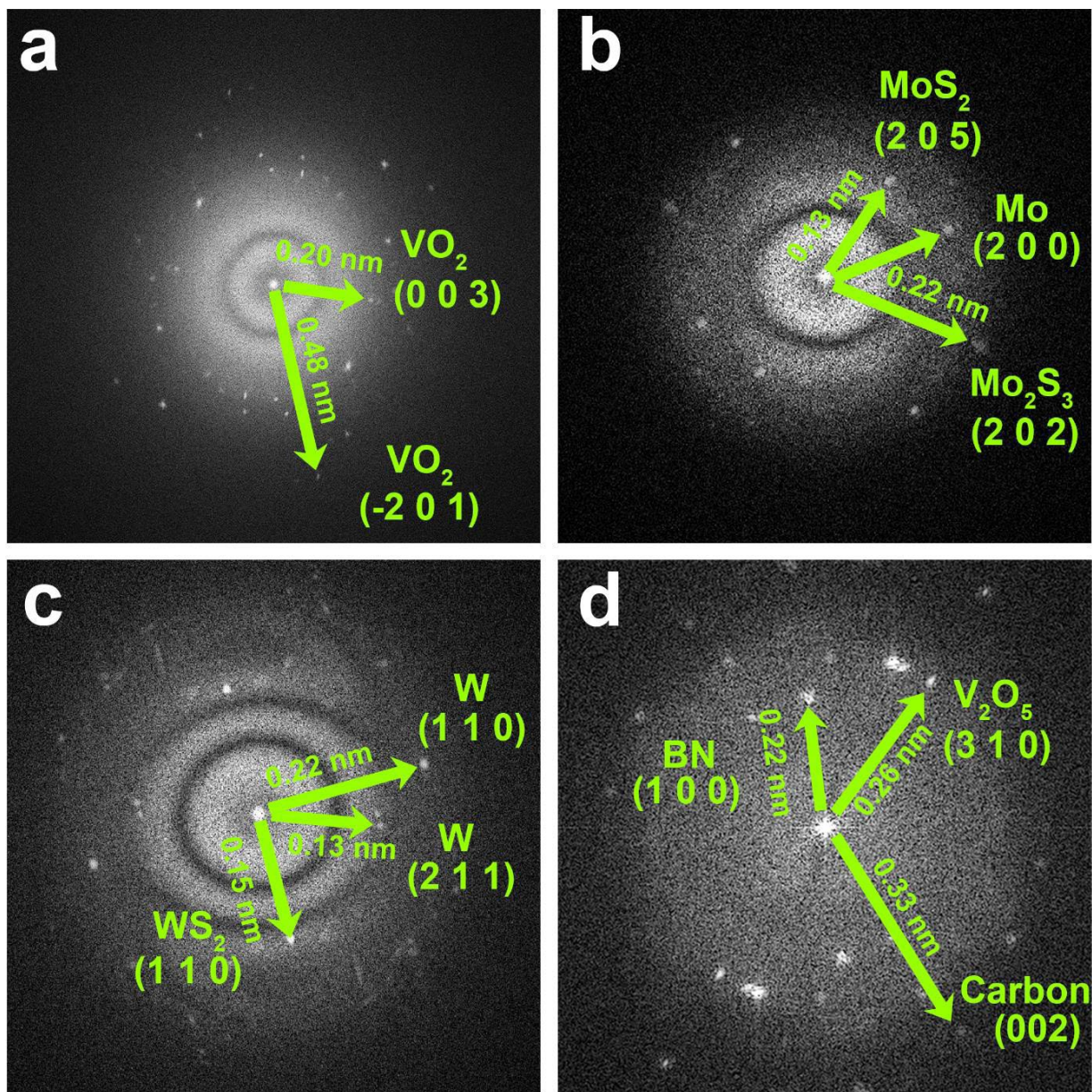
Fig. S10. FFT spectra of (a) V_xO_y, (b) Mo_xS_y, (c) W_xS_y nanosheets, and (d) BN/V_2O_5/C heterostructure nanosheets, respectively.
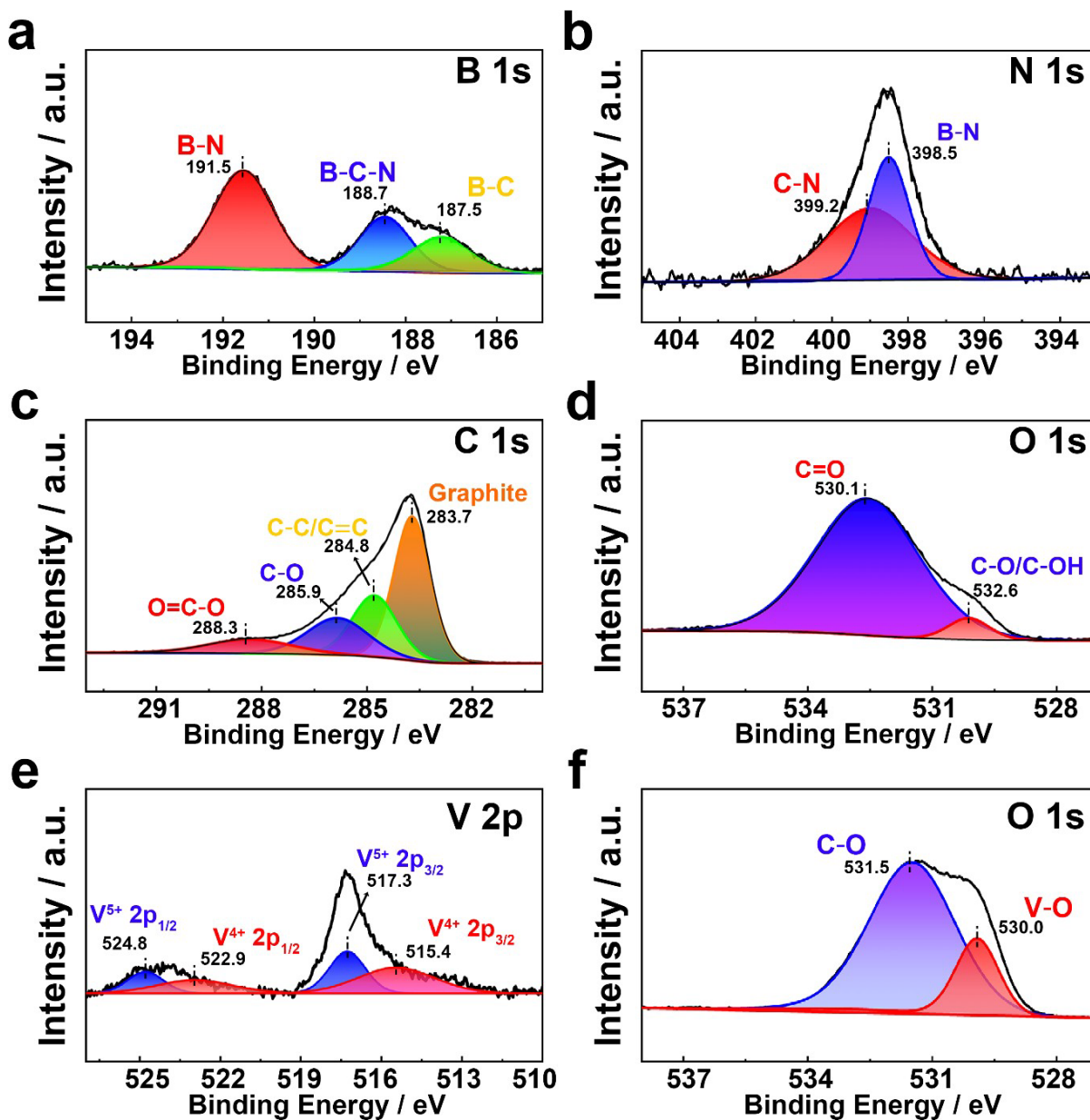
Fig. S11. XPS spectra of BN nanosheets, (a) B 1s, and (b) N 1s. XPS spectra of Carbon nanosheets, (c) C 1s, and (d) O 1s. XPS spectra of V_xO_y nanosheets, (e) V 2p, and (f) O 1s.

The XPS analysis results of BN nanosheets (Fig. S11(a and b)) indicate that the BN nanosheets are mainly composed of B and N. The B 1s peaks centered at around 191.5, 188.7 and 187.5 eV, correspond to the B-N, B-C-N and B-C,[13] and the two fitted peaks centered at 399.2 eV and 398.5 eV in the N 1s spectrum (Fig. S11b) are assigned to C-N and B-N groups.[14] Fig. S11c show the C 1s peaks centered at around 288.3, 285.9, 284.8 and 283.7 eV, correspond to the C-C/C=C, C-O and O=C-O, and the peak at 283.7 eV is assigned to graphite,[15] indicating the successful preparation of carbon nanosheets. The XPS results of V_xO_y nanosheets (Fig. S11e) show that V 2p spectra possess two distinct

peaks with binding energy at 522.9 eV and 515.4 eV, which are in accordance with V $2p_{1/2}$ and V $2p_{3/2}$, respectively. The blue shadow of the peaks located at 524.8 and 517.3 eV are attributed to the V^{5+}, which are in accordance with V $2p_{1/2}$ and V $2p_{3/2}$.[16] The O1s spectra (Fig. S11f) can be split into two peaks at 530.0 eV and 531.5 eV, corresponding to V-O and C-O, respectively.[17]
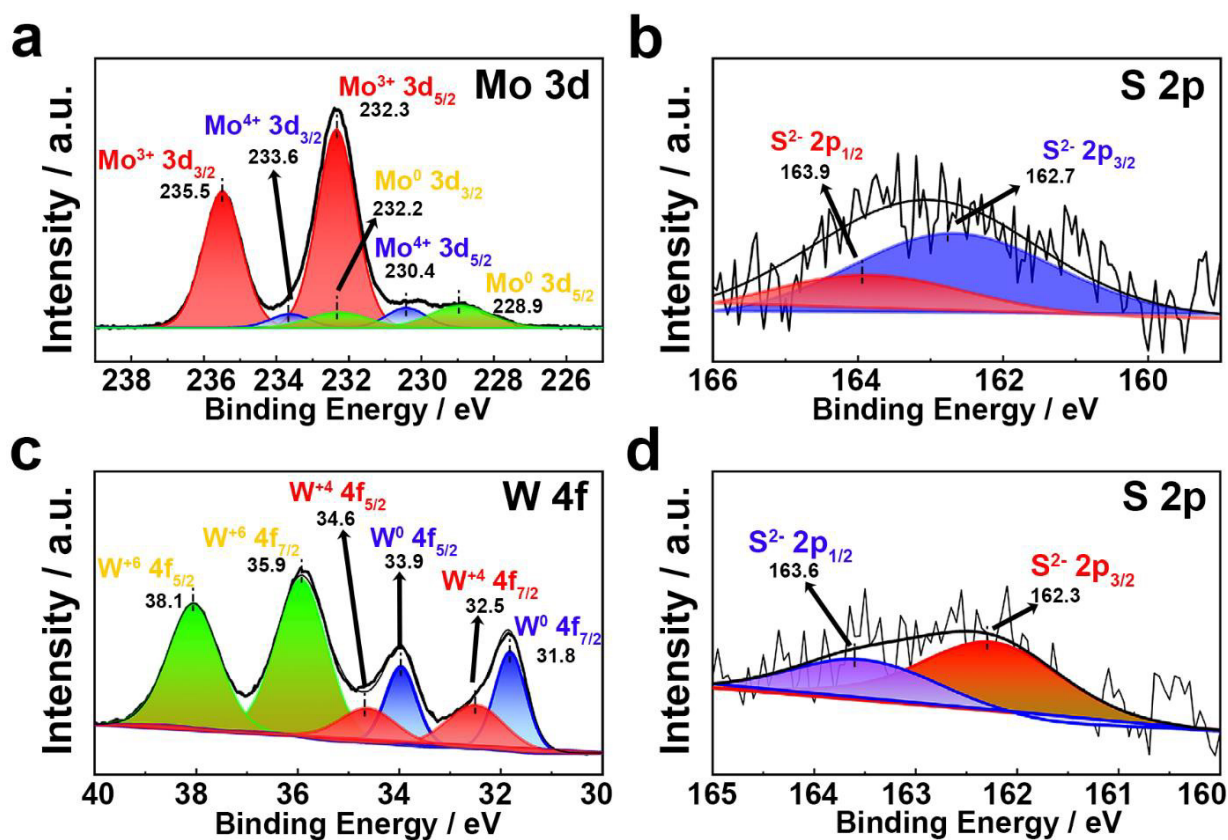

Fig. S12. XPS spectra of Mo_xS_y nanosheets, (a) Mo 3d, and (b) S 2p. XPS spectra of W_xS_y nanosheets, (c) W 4f, and (d) S 2p.

The XPS results of Mo_xS_y nanosheets (Fig. S12a) show that Mo $3d_{5/2}$ and Mo $3d_{3/2}$ with binding energies at about 232.3 and 235.5 eV, respectively, confirm the formation of Mo_2S_3 nanosheets,[18] while the peaks nearly 233.6 eV and 230.4 eV correspond to +4 state of Mo $3d_{3/2}$ and Mo $3d_{5/2}$, indicating the presence of MoS_2 nanosheets,[19] The peaks at 232.2 eV and 228.9 eV are related to the Mo $3d_{3/2}$ and Mo $3d_{5/2}$ binding energies, respectively, corresponding to the Mo metal.[20] Moreover, the XPS peaks (Fig. S12b) at 162.7 eV and 163.9 eV are attributed to the binding energy for S $2p_{3/2}$ and S $2p_{1/2}$ respectively, which are mainly characteristic of S^{2-} of Mo_2S_3 and MoS_2 nanosheets.[21]

The XPS spectrum (Fig. S12c) shows the binding energies of the W $4f_{7/2}$ and W $4f_{5/2}$ peaks at 32.5 and 34.6 eV, respectively, which are typical values for W^{4+} in WS_2 nanosheets.[22] The peaks at 31.8 eV and 33.9 eV are related to the W $4d_{7/2}$ and W $4f_{5/2}$ binding energies, respectively, corresponding to the W metal.[23] Furthermore, in Fig. S12d, the characteristic peaks at 162.3 and 163.6 eV in the core level spectrum of S correspond to S $2p_{3/2}$ and S $2p_{1/2}$ binding energies, respectively. Besides, the presence of other peaks is due to the unavoidable oxidation and CO_2 adsorption of nanosheets in air.[24]
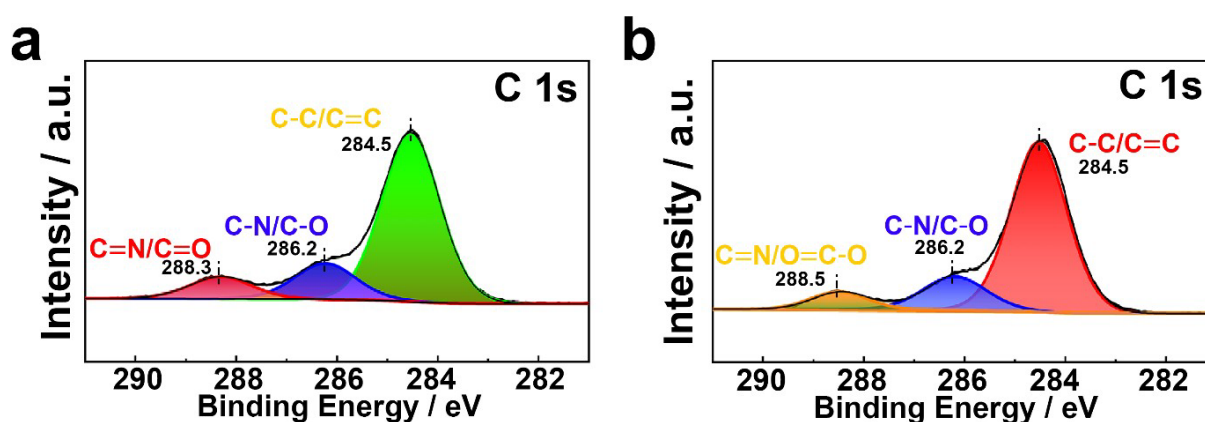

Fig. S13. XPS spectra of $BN/V_2O_5/C$ heterostructure nanosheets, (a) C 1s. XPS spectra of $BN/Mo_xS_y/C$ heterostructure nanosheets, (b) C 1s.
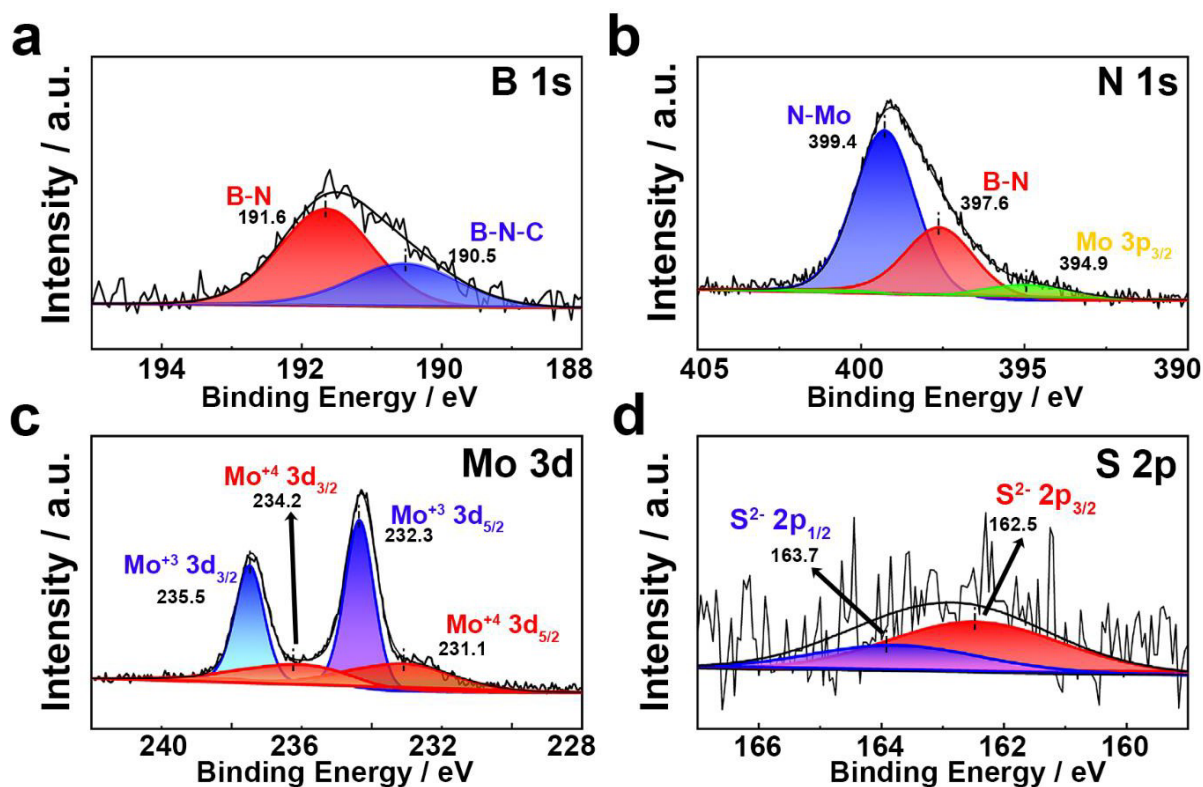
Fig. S14. XPS spectra of BN/Mo$_x$S$_y$/C heterostructure nanosheets. (a) B 1s, (b) N 1s, (c) Mo 3d, and (d) S 2p.

The XPS results of BN/Mo$_x$S$_y$/C heterostructure nanosheets (Fig. S14a) show the B 1s peaks can be resolved into ve components centered at around 191.6 and 190.5 eV, and the peak of 191.6 eV corresponding to the B-N.[25] It can be B-N-C moiety (190.5 eV) in BN.[26] The three fitted peaks at 399.4 eV, 397.6 eV and 394.9eV in the N 1s spectrum (Fig. S14b) were assigned to N-Mo,[27] B-N groups and Mo 3p$_{3/2}$. The peak at 394.9 eV is attributed to the N-Mo bond, indicating a strong coupling C-N-Mo bond between the C-N bond and N-Mo bond.[28] The Mo 3d peaks (Fig. S14c), Mo 3d$_{5/2}$ and Mo 3d$_{3/2}$ with binding energies at about 232.3 and 235.5 eV, respectively, confirming the existence of Mo$_2$S$_3$. The peaks nearly 234.2 eV and 231.1 eV corresponding to +4 state of Mo 3d$_{3/2}$ and Mo 3d$_{5/2}$, indicates the presence of MoS$_2$. The S 2p signals (Fig. S14d) were split into two doublets of S 2p$_{3/2}$ and S 2p$_{1/2}$ with binding energies observed at 162.5 and 163.7 eV corresponds to S^{2-} respectively. Fig. S13b shows the C1s peaks which can be resolved into ve components centered at around 288.5, 286.2, 284.5 eV, corresponding to O=C-O/C=N,[29] C-O/C-N,[30] C-C/C=C,[31] and the C 1s peak for sp^2-hybridized carbon usually appears near 284.5 eV for pure graphite powder. The peak of the C=N and the C-N bond, indicates a strong coupling

effect between carbon nanosheets and BN nanosheets, and successful preparation of BN/Mo$_x$S$_y$/C heterostructures.
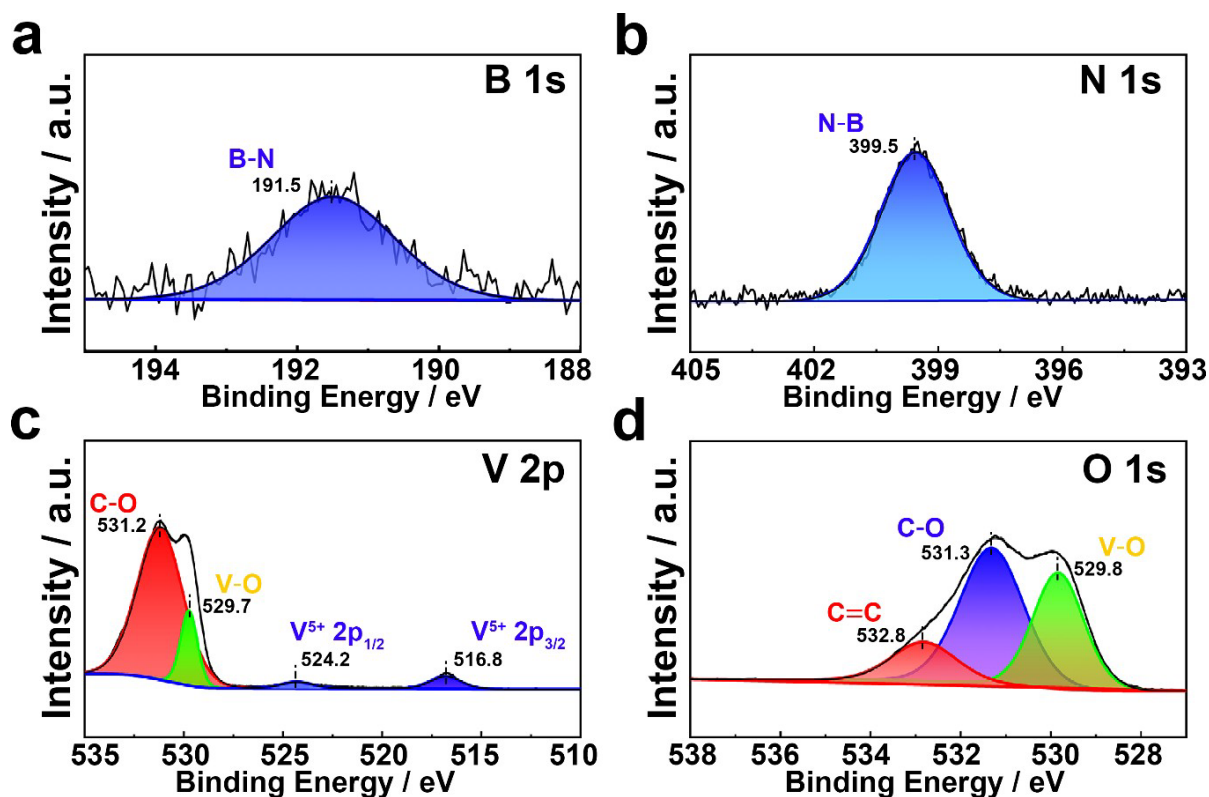

Fig. S15. XPS spectra of BN/V$_2$O$_5$/C heterostructure nanosheets. (a) B 1s, (b) N 1s, (c) V 2p, and (d) O 1s.

Similarly, the XPS results of BN/V$_2$O$_5$/C heterostructure nanosheets (Fig. S15) show the V 2p spectra possess two distinct peaks with binding energy at 524.2 eV and 516.8 eV, which are in accordance with V 2p$_{1/2}$ and V 2p$_{3/2}$, the peaks at 531.2 and 529.7 eV are attributed to the C-O bond and V-O bond, and the binding energy at 399.5 eV is referred to N-B bonds.[32] The peaks at 529.8 and 532.8 eV are attributed to the V-O bond and carbonyl groups (C=O),[33] and 531.3 eV corresponds to C-O bond, respectively. The C 1s peaks (Fig. S13a) which can be resolved into ve components centered at around 288.3, 286.2 and 284.5 eV, corresponding to O=C-O/C=N,[34] C-O/C-N,[35] C-C/C=C,[36] the C1s peak for sp^2-hybridized carbon usually appears near 284.5 eV for pure graphite powder. The peaks of the C=N and the C-N bond, indicate a strong coupling effect between carbon nanosheets and BN nanosheets.
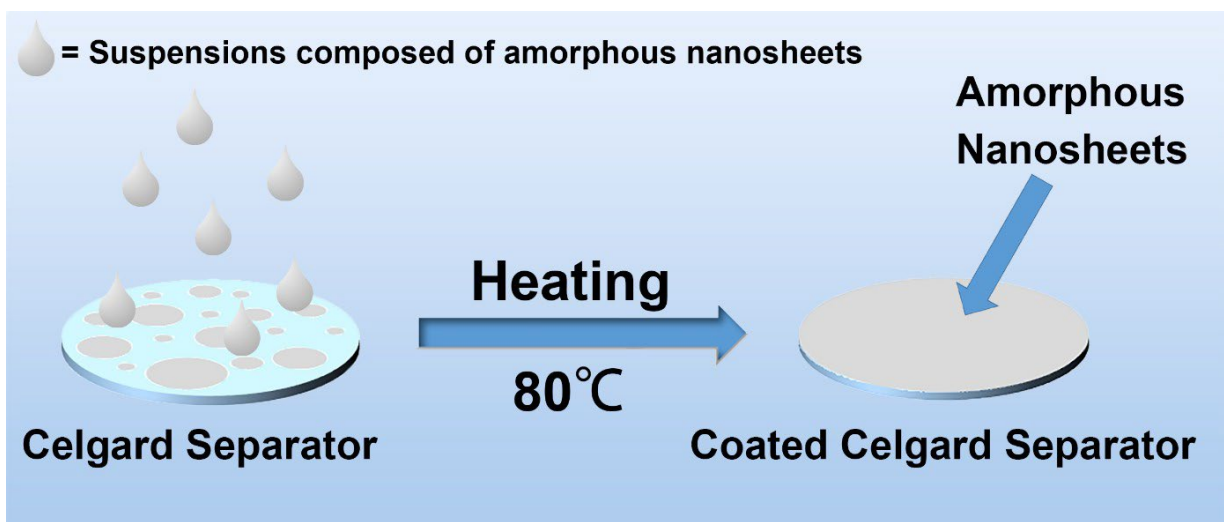
Fig. S16. Schematic diagrams for the fabrication of coated separators.
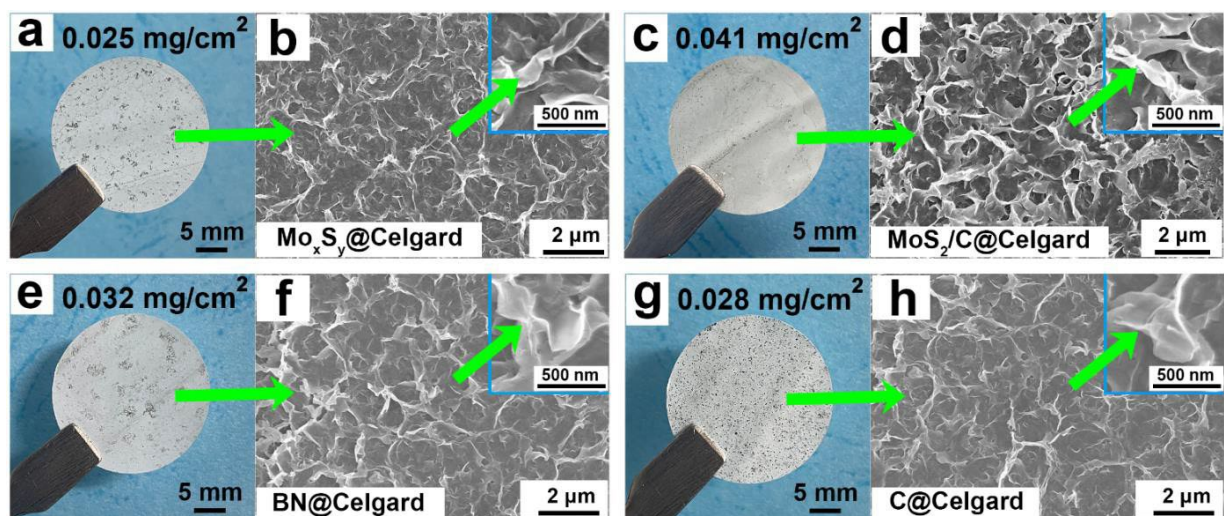
Fig. S17. The SEM and digital images of the modified separator. (a,b) Mo_xS_y@Celgard, (c,d) MoS_2/C@Celgard, (e,f) BN@Celgard, and (g,h) C@Celgard separators, respectively.

Table S1. Synthesis of 2D amorphous nanomaterials

Material category	Yield	Solvents	Preparation process	Reference
Amorphous BN, Mo_xS_y, V_xO_y, W_xS_y, C, BN/C, MoS_2/C, V_2O_5/C, WS_2/C, BN/Mo_xS_y/C, BN/V_2O_5/C Nanosheets	**97.5 %**	Pure water **(No chemicals, no toxic, low cost)**	Ball-milling insertion and pure-water exfoliation **(At room temperature, simple process)**	This Work
BN nanosheets	70 % - 76 %	ethanol	First, The BN exfoliation was carried out using a microfluidizer at 125 MPa for 50 cycles; second, after exfoliation followed by standing for 7 days (Need complicated device, and long-time)	[37]
Amorphous Al_2O_3 Nanosheets		NH_4HCO_2 and CH_2O_2 (Expensive and toxic)	650 °C for 2 h under an air atmosphere (Need high temperature and inert atmosphere)	[38]
MoS_2 nanosheets	80 %	Py-Li, Nap-Li, DME (Expensive and toxic)	First, vacuum drying; second, sonication; finally, centrifuged at 12000 rpm (Need vacuum environment and high speed centrifugation)	[39]

Amorphous $Ni_{1-x}Fe_x$ Nanosheets		HCl solution (Toxic)	Prepared by electrodeposition using a three-electrode cell (Need complicated device and process)	[40]
MoS_2 Nanosheets	92 %			
TaS_2 Nanosheets	93 %	$LiPF_6$ (Expensive and toxic)	First, the electrochemical intercalation of Li ions into layered inorganic crystals; second, sonication process (Complicated process)	[41]
TiS_2 Nanosheets	93 %			
MoS_2 nanosheets	68 %	$(NH_4)_6Mo_7O_{24} \cdot 4H_2O$, K_2S, LiCl, KCl (Expensive and toxic)	CVD (Need high temperature and inert atmosphere)	[42]
Amorphous SnO_x Nanosheets		$C_4H_{10}O_3$ (Expensive and toxic)	180 °C with the oxygen gas at a rate of 100 sccm (Need high temperature and O_2 atmosphere)	[43]

Sb nanosheets	90 %	Concentrated hydrochloric acid and ethanol (Toxic and dangerous)	First, 300 °C for 5 h; second, concentrated hydrochloric acid remove the remaining impurities (Need high temperature. And the process is dangerous)	[44]
Amorphous FeP@CNs Nanosheets		Phytic acid and HCl (Expensive and toxic)	900 °C for 1 h under an Ar atmosphere (Need temperature and Ar atmosphere)	[45]
In_2Se_3 nanosheets	83 %	α-In_2Se_3 and DMF (Expensive and toxic)	Electrochemical intercalation method (Need complicated device and process)	[46]
Amorphous Cr_2O_3 Nanosheets		Cu_2O-oleate complex intermediate and ethanol (Expensive)	First, dried in vacuum for 2 h; second, 300 °C for 1 h in air atmosphere (Need high temperature and vacuum environment)	[47]
Amorphous Mo_2C Nanosheets		CH_3CSNH_2 (Expensive and toxic)	First, ball-milling for 13 h at 900 rpm; second, 180 °C under the pressure of 20 bar for 1 h (Need high temperature, high speed, and high pressure)	[48]

$Ti_3C_2T_x$ Nanosheets	81.4 %	LiF, HCl, HF (Expensive and toxic)	First, freeze-and-thaw; second, sonication treatment (Need N_2, O_2, and liquid nitrogen. And the process is complicated)	[49]
Amorphous V_2O_5/Graphene Nanosheets		$H_2C_2O_4$ (Toxic) single-layer graphene oxide (Expensive)	First, 75 °C for 2 h; second, the resultant solution was frozen by liquid nitrogen, and then freeze-dried for 3 days; finally, annealed at 300 °C for 3 h (Need high temperature. And the process is complicated)	[50]
Graphene	40 %	No Chemicals	Plasma spraying (Need complicated device and harsh conditions. The process is complicated)	[51]
Amorphous g-C_3N_4 Nanosheets		PVP and H_2O_2 (Expensive and toxic)	First, CO_2 was injected to reach 20 MPa and kept at 80 °C for 4 h; second, centrifuged at 20000 rpm (Need high temperature, CO_2 atmosphere, high pressure and speed centrifugation)	[52]

Table S2. Comparison of electrochemical performance of present work with various functional interlayers **(1 C= 1675 mA g^{-1})**

Separators		Li-S cells		Reference
Coating layer	**Thickness (μm)**	**Rate performance [mAh g^{-1}] /current density**	**Initial capacity [mAh g^{-1}] /current density**	
BN/Mo$_x$S$_y$/C	**0.37**	**1568/ 0.2 A g^{-1} (0.12 C)** **1280/ 0.5 A g^{-1} (0.30 C)** **1165/ 1.0 A g^{-1} (0.60 C)** **1093/ 2.0 A g^{-1} (1.20 C)** **656/ 5.0 A g^{-1} (3.0 C)**	**1407/ 1 A g^{-1} (0.60 C)**	**This work**
a-Fe$_3$O$_{4-x}$/GO	N/A	1395/ 0.1 C 890/ 0.2 C 811/ 0.5 C 648/ 1.0 C	1313/ 0.1 C	[53]
MQD@NG	11.5	1227/ 0.2 C 1075/ 0.5 C 952/ 1.0 C	1230/ 0.2 C	[54]
SCOF-2	70	1235/ 0.1 C 950/ 0.2 C 746/ 0.5 C 642/ 1.0 C 536/ 2.0 C	1036/ 0.2 C	[55]
Janus-S	20	1244/ 0.1 C 1080/ 0.2 C 862/ 0.5 C 692/ 1.0 C 583/ 2.0 C	1203/ 0.2 C	[56]
Ti$_3$C$_2$@iCON	5	1280/ 0.1 C 1186/ 0.2 C 1048/ 0.5 C 956/ 1.0 C		[57]
CSG/S	10	1150/ 0.2 C 1085/ 0.5 C 1015/ 1.0 C	1325 / 0.2 C	[58]
ANF-JS30s	26	912/ 0.2 C 782/ 0.5 C 700/ 1.0 C 633/ 2.0 C	857/ 0.5 C	[59]

SrF$_2$-G	22	1311/ 0.1 C 1223/ 0.2 C 1131/ 0.5 C 1083/ 1.0 C	1124/ 0.5 C	[60]
HAI	8	1039/ 0.2 C 862/ 0.5 C 688/ 1.0 C	983/ 0.5 C	[61]
V$_2$C/V$_2$O$_5$	10	1231/ 0.2 C 1103/ 0.5 C 1050/ 1.0 C	1240/ 0.2 C	[62]
CoPc@GO	0.2	1450/ 0.2 C 912/ 0.5 C 705/ 1.0 C 455/ 2.0 C	992/ 0.5 C	[63]
RPM	2.5	1364/ 0.1 C		[64]
FM@G	37.5	1082/ 1.0 C		[65]
N-Co$_2$VO$_4$-Co	6.5	1522/ 0.1 C	1401/ 0.2 C	[66]
CoFe@NC	8	1473/ 0.1 C 1034/ 0.2 C 883/ 0.5 C 806/ 1.0 C	890/ 0.5 C	[67]
Ti$_3$C$_2$T$_x$/Ni-Co MOF	4.5	1340/ 0.1 C 1170/ 0.2 C 100/ 0.5 C 820/ 1.0 C 660/ 2.0 C	1010/ 0.5 C	[68]
Ni$_{0.2}$Mo$_{0.8}$N/M WCNT	N/A	1421/ 0.1 C 900/ 0.2 C 766/ 0.5 C 694/ 1.0 C 632/ 2.0 C		[69]
TaVG	1.5	1069/ 1.0 C	1118/ 0.5 C	[70]
MnS/N-C@CNT	6	1181/ 0.1 C 890/ 0.5 C 890/ 1.0 C 500/ 2.0 C	924/ 0.5 C	[71]
Ni-Co-P@C	3.2	1412/ 0.1 C 1093/ 0.2 C 961/ 0.5 C 906/ 1.0 C		[72]

Reference

[1] M. Du, X. Li, A. Wang, Y. Wu, X. Hao, M. Zhao, *Angewandte Chemie International Edition*, 2014, **53**, 3645-3649.

[2] S. Thiagarajan, M. Thaiyan, R. Ganesan, *RSC Advances*, 2016, **6**, 82581-82590.

[3] L. Niu, K. Li, H. Zhen, Y.-S. Chui, W. Zhang, F. Yan, Z. Zheng, *Small*, 2014, **10**, 4651-4657.

[4] C.E. Lim, M.L. Ooi, R.C.S. Wong, K.E. Neo, A. Mumtaz, M. Mazhar, N.M. Mohamed, M.S.M. Saheed, *Applied Nanoscience*, 2019, **9**, 1281-1292.

[5] H. Li, Q. Zhang, C.C.R. Yap, B.K. Tay, T.H.T. Edwin, A. Olivier, D. Baillargeat, *Advanced Functional Materials*, 2012, **22**, 1385-1390.

[6] C. Hontoria-Lucas, A.J. López -Peinado, J.d.D. López -Gonzále z, M.L. Rojas-Cervantes, R.M. Martín -Aranda, *Carbon*, 1995, **33**, 1585-1592.

[7] S. Chen, R. Xu, J. Liu, X. Zou, L. Qiu, F. Kang, B. Liu, H.-M. Cheng, *Advanced Materials*, 2019, **31**, 1804810.

[8] F. Huguenin, E.A. Ticianelli, R.M. Torresi, *Electrochimica Acta*, 2002, **47**, 3179-3186.

[9] H.S. Vaziri, A. Shokuhfar, S.S.S. Afghahi, *Materials Research Express*, 2020, **7**, 025034.

[10] K. Kasinathan, K. Marimuthu, B. Murugesan, M. Sathaiah, P. Subramanian, P. Sivakumar, U. Swaminathan, R. Subbiah, *International Journal of Biological Macromolecules*, 2021, **190**, 520-532.

[11] Y. Chen, Z. Xiang, D. Wang, J. Kang, H. Qi, *RSC Advances*, 2020, **10**, 23936-23943.

[12] T. Naresh Kumar, N. Chandrasekaran, K. Lakshminarasimha Phani, *Chemical Communications*, 2015, **51**, 5052-5055.

[13] S.Y. Kim, J. Park, H.C. Choi, J.P. Ahn, J.Q. Hou, H.S. Kang, *Journal of the American Chemical Society*, 2007, **129**, 1705-1716.

[14] K. Raidongia, A. Nag, K.P.S.S. Hembram, U.V. Waghmare, R. Datta, C.N.R. Rao, *Chemistry - A European Journal*, 2010, **16**, 149-157.

[15] Y. Li, W. Gao, L. Ci, C. Wang, P.M. Ajayan, *Carbon*, 2010, **48**, 1124-1130.

[16] C. Zhang, S.-H. Park, S.E. O'Brien, A. Seral-Ascaso, M. Liang, D. Hanlon, D. Krishnan, A. Crossley, N. McEvoy, J.N. Coleman, V. Nicolosi, *Nano Energy*, 2017, **39**, 151-161.

[17] H. Luo, B. Wang, C. Wang, F. Wu, F. Jin, B. Cong, Y. Ning, Y. Zhou, D. Wang, H. Liu, S. Dou, *Energy Storage Materials*, 2020, **33**, 390-398.

[18] Q. Pan, Y. Liu, L. Zhao, *Chemical Engineering Journal*, 2018, **351**, 603-612.

[19] L. Guo, L. Ji, J. Wang, S. Zuo, Z. Chen, *ACS Applied Materials & Interfaces*, 2018, **10**, 36824-36833.

[20] J. Baltrusaitis, B. Mendoza-Sanchez, V. Fernandez, R. Veenstra, N. Dukstiene, A. Roberts, N. Fairley, *Applied Surface Science*, 2015, **326**, 151-161.

[21] D. Dinda, M.E. Ahmed, S. Mandal, B. Mondal, S.K. Saha, *Journal of Materials Chemistry A*, 2016, **4**, 15486-15493.

[22] Y. Yue, J. Chen, Y. Zhang, S. Ding, F. Zhao, Y. Wang, D. Zhang, R. Li, H. Dong, W. Hu, Y. Feng, W. Feng, *ACS Applied Materials & Interfaces*, 2018, **10**, 22435-22444.

[23] R. Bhandavat, L. David, G. Singh, *The Journal of Physical Chemistry Letters*, 2012, **3**, 1523-1530.

[24] J.-H. Cha, S.-J. Choi, S. Yu, I.-D. Kim, *Journal of Materials Chemistry A*, 2017, **5**, 8725-8732.

[25] N.K. Singh, K. Pramoda, K. Gopalakrishnan, C.N.R. Rao, *RSC Advances*, 2018, **8**, 17237-17253.

[26] S. Baik, J.W. Lee, *RSC Advances*, 2015, **5**, 24661-24669.

[27] S. Liu, H. Zhu, W. Yao, K. Chen, D. Chen, *Applied Surface Science*, 2018, **430**, 309-315.

[28] S. Guo, H. Yang, M. Liu, X. Feng, H. Xu, Y. Bai, C. Wu, *ACS Applied Energy Materials*, 2021, **4**, 7064-7072.

[29] H. Xu, L. Qin, J. Chen, Z. Wang, W. Zhang, P. Zhang, W. Tian, Y. Zhang, X. Guo, Z. Sun, *Journal of Materials Chemistry A*, 2018, **6**, 13153-13163.

[30] J. Ederer, P. Janoš, P. Ecorchard, J. Tolasz, V. Štengl, H. Beneš, M. Perchacz, O. Pop-Georgievski, *RSC Advances*, 2017, **7**, 12464-12473.

[31] C. Zheng, S. Niu, W. Lv, G. Zhou, J. Li, S. Fan, Y. Deng, Z. Pan, B. Li, F. Kang, Q.-H. Yang, *Nano Energy*, 2017, **33**, 306-312.

[32] C. Huang, C. Chen, X. Ye, W. Ye, J. Hu, C. Xu, X. Qiu, *Journal of Materials Chemistry A*, 2013, **1**, 12192-12197.

[33] Z. Ding, Y. Cui, D. Wan, H. Luo, Y. Gao, *RSC Advances*, 2017, **7**, 29496-29504.

[34] S. Gao, X. Yang, M.-J. Wei, S. Liang, H.-Y. Zang, H.-Q. Tan, Y.-H. Wang, Y.-G. Li, *New Journal of Chemistry*, 2018, **42**, 198-203.

[35] W. Lu, X. Qin, S. Liu, G. Chang, Y. Zhang, Y. Luo, A.M. Asiri, A.O. Al-Youbi, X. Sun, *Analytical Chemistry*, 2012, **84**, 5351-5357.

[36] W. Yang, W. Yang, A. Song, G. Sun, G. Shao, *Nanoscale*, 2018, **10**, 816-824.

[37] Q. Yan, W. Dai, J. Gao, X. Tan, L. Lv, J. Ying, X. Lu, J. Lu, Y. Yao, Q. Wei, R. Sun, J. Yu, N. Jiang, D. Chen, C.-P. Wong, R. Xiang, S. Maruyama, C.-T. Lin, *ACS Nano*, 2021, **15**, 6489-6498.

[38] Z. Yang, S. Zhang, H. Zhao, A. Li, L. Luo, L. Guo, *ACS Catalysis*, 2021, **11**, 11542-11550.

[39] X. Zhu, Z. Su, C. Wu, H. Cong, X. Ai, H. Yang, J. Qian, *Nano Letters*, 2022, **22**, 2956-2963.

[40] B.B. Gicha, L.T. Tufa, Y. Choi, J. Lee, *ACS Applied Energy Materials*, 2021, **4**, 6833-6841.

[41] R. Yang, L. Mei, Q. Zhang, Y. Fan, H.S. Shin, D. Voiry, Z. Zeng, *Nature Protocols*, 2022, **17**, 358-377.

[42] H. Jin, Z. Hu, T. Li, L. Huang, J. Wan, G. Xue, J. Zhou, *Advanced Functional Materials*, 2019, **29**, 1900649.

[43] T. Yuan, Z. Hu, Y. Zhao, J. Fang, J. Lv, Q. Zhang, Z. Zhuang, L. Gu, S. Hu, *Nano Letters*, 2020, **20**, 2916-2922.

[44] L. Yi, J. Chen, P. Shao, J. Huang, X. Peng, J. Li, G. Wang, C. Zhang, Z. Wen, *Angewandte Chemie International Edition*, 2020, **59**, 20112-20119.

[45] Z. Zheng, H.-H. Wu, H. Liu, Q. Zhang, X. He, S. Yu, V. Petrova, J. Feng, R. Kostecki, P. Liu, D.-L. Peng, M. Liu, M.-S. Wang, *ACS Nano*, 2020, **14**, 9545-9561.

[46] H. Shi, M. Li, A. Shaygan Nia, M. Wang, S. Park, Z. Zhang, M.R. Lohe, S. Yang, X. Feng, *Advanced Materials*, 2020, **32**, 1907244.

[47] B. Jia, J. Yang, R. Hao, L. Li, L. Guo, *ACS Materials Letters*, 2020, **2**, 610-615.

[48] C. Du, B. Yan, G. Yang, *Nano Energy*, 2020, **76**, 105031.

[49] X. Huang, P. Wu, A Facile, *Advanced Functional Materials*, 2020, **30**, 1910048.

[50] X. Wang, Y. Li, S. Wang, F. Zhou, P. Das, C. Sun, S. Zheng, Z.-S. Wu, *Advanced Energy Materials*, 2020, **10**, 2000081.

[51] A. Islam, B. Mukherjee, K.K. Pandey, A.K. Keshri, *ACS Nano*, 2021, **15**, 1775-1784.

[52] L. Du, Q. Tian, X. Zheng, W. Guo, W. Liu, Y. Zhou, F. Shi, Q. Xu, *Energy & Environmental Materials*, 2021.

[53] Y. Zhao, J. Liu, Y. Zhou, X. Huang, Q. Liu, F. Chen, H. Qin, H. Lou, D.Y.W. Yu, X. Hou, *ACS Applied Materials & Interfaces*, 2021, **13**, 41698-41706.

[54] B. Yu, D. Chen, Z. Wang, F. Qi, X. Zhang, X. Wang, Y. Hu, B. Wang, W. Zhang, Y. Chen, J. He, W. He, *Chemical Engineering Journal*, 2020, **399**, 125837.

[55] J. Xu, S. An, X. Song, Y. Cao, N. Wang, X. Qiu, Y. Zhang, J. Chen, X. Duan, J. Huang, W. Li, Y. Wang, *Advanced Materials*, 2021,**33**, 2105178.

[56] Y. Li, T. Gao, D. Ni, Y. Zhou, M. Yousaf, Z. Guo, J. Zhou, P. Zhou, Q. Wang, S. Guo, *Advanced Materials*, 2022, **34**, 2107638.

[57] P. Li, H. Lv, Z. Li, X. Meng, Z. Lin, R. Wang, X. Li, *Advanced Materials*, 2021, **33**, 2007803.

[58] Z. Zhang, Y. Dong, Y. Gu, P. Lu, F. Xue, Y. Fan, z. Zhu, J. Lin, Q. Li, Z.-S. Wu, *Journal of Materials Chemistry A*, 2022.

[59] H. Pei, C. Yang, Q. Wu, X. Zhou, X. Xie, B. Hwang, Y. Ye, *Journal of Materials Chemistry A*, 2022,**10**, 5317-5327.

[60] W. Jing, J. Zu, K. Zou, X. Dai, Y. Song, J. Han, J. Sun, Q. Tan, Y. Chen, Y. Liu, *Journal of Materials Chemistry A*, 2022,**10**, 4833-4844.

[61] D.W. Kim, C. Senthil, S.M. Jung, S.-S. Kim, H.-S. Kim, J.W. Hong, J.-H. Ahn, H.Y. Jung, *Energy Storage Materials*, 2022, **47**, 472-481.

[62] T. Wang, Y. Liu, X. Zhang, J. Wang, Y. Zhang, Y. Li, Y. Zhu, G. Li, X. Wang, *ACS Applied Materials & Interfaces*, 2021, **13**, 56085-56094.

[63] C. Shen, Y. Li, M. Gong, C. Zhou, Q. An, X. Xu, L. Mai, *ACS Applied Materials & Interfaces*, 2021, **13**, 60046-60053.

[64] M. Shi, Z. Liu, S. Zhang, S. Liang, Y. Jiang, H. Bai, Z. Jiang, J. Chang, J. Feng, W. Chen, H. Yu, S. Liu, T. Wei, Z. Fan, *Advanced Energy Materials*, 2022, 2103657.

[65] Z. Cheng, Y. Chen, Y. Yang, L. Zhang, H. Pan, X. Fan, S. Xiang, Z. Zhang, *Advanced Energy Materials*, 2021, **11**, 2003718.

[66] W. Zhou, D. Zhao, Q. Wu, J. Dan, X. Zhu, W. Lei, L.-J. Ma, L. Li, *Small*, 2021, **17**, 2104109.

[67] Y. Wang, L. Zhu, J. Wang, Z. Zhang, J. Yu, Z. Yang, *Chemical Engineering Journal*, 2022,**433**, 133792.

[68] Y. Ren, Q. Zhai, B. Wang, L. Hu, Y. Ma, Y. Dai, S. Tang, X. Meng, *Chemical Engineering Journal*, 2022, **439**, 135535.

[69] H. Zhang, R. Dai, S. Zhu, L. Zhou, Q. Xu, Y. Min, *Chemical Engineering Journal*, 2022, **429**, 132454.

[70] Q. Zhao, R. Wang, J. Wen, X. Hu, Z. Li, M. Li, F. Pan, C. Xu, *Nano Energy*, 2022, **95**, 106982.

[71] F. Li, X. Qian, L. Jin, *ACS Sustainable Chemistry & Engineering*, 2021, **9**, 15469-15477.

[72] Z. Wu, S. Chen, L. Wang, Q. Deng, Z. Zeng, J. Wang, S. Deng, *Energy Storage Materials*, 2021, **38**, 381-388.